Mon. Not. R. astr. Soc. (1987) **228**, 973–991

Mass deposition in cooling flows – analysis of the X-ray data

P. A. Thomas and A. C. Fabian *Institute of Astronomy, Madingley Road, Cambridge CB3 0HA*

P. E. J. Nulsen *Mt Stromlo and Siding Spring Observatories, Private Bag, Woden PO, ACT 2606, Australia*

Accepted 1987 May 27. Received 1987 May 27; in original form 1987 March 10

Summary. We present a 'multiphase method' for the analysis of X-ray data of the cooling inflow region of intracluster gas in clusters of galaxies. The method employs a range of densities at each radius and treats the mass-deposition from the flow in a self-consistent way. We find good agreement between results from this multiphase method and those obtained with our previous, single-phase approach which assumed only one characteristic density at each radius. For the best data-sets the density distribution of the various phases agrees with theoretical expectations only if a massive halo is added to the gravitational potential of the central galaxy. We present mass deposition profiles, $\dot{M}(<r)$, of those clusters for which our method is applicable. These rise linearly with radius and reach values of up to 100 $M_\odot$ yr^{-1} within 100 kpc.

1 Introduction

Cooling flows deposit significant amounts of cold gas in the centres of many clusters of galaxies (Fabian, Nulsen & Canizares 1984; Sarazin 1986). The hot intracluster gas cools through emission of X-rays and deposits cooled gas at rates of up to 1000 $M_\odot$ yr^{-1} over a wide range of radii in a manner consistent with the formation of a large galaxy. A study of the X-ray data of over 40 cooling flows by Arnaud (1985; also Arnaud & Fabian 1987) shows that the mass deposition rate within radius r, $\dot{M}(<r)$, is closely proportional to r within the region where the radiative cooling time, $t_{\rm cool}$, is less than the Hubble time, H_0^{-1}. This cooling region is typically 100–200 kpc in radius.

A range of densities must be present throughout the flow for matter to be deposited at different radii. A homogeneous flow leads to a central singularity whereas in a non-uniform flow thermal instability amplifies density variations and causes the gas to cool at finite radii. Very little matter need then reach the centre. Previous studies have assumed that the gas at each radius has a single temperature and density. Although this is an oversimplification, we show here that it gives results in fair agreement with a more comprehensive treatment. One of us (Paper I, Nulsen 1986) has carried out a theoretical study of non-uniform cooling flows in which a continuous density

distribution occurs at all radii. Here (Paper II), we attempt to analyse the data in the spirit of that study and employ as many phases within each shell as there are shells within that radius. This produces a self-consistent model which makes the maximum use of the data. Our major interests are the form of the mass deposition profile and the initial density distribution of the gas. Other theoretical approaches have had to assume some prescription for the manner in which the matter drops out of the flow (Thomas 1986; White & Sarazin 1987a,b).

2 The cluster sample and deprojection of the data

All of the X-ray data that we use were obtained with the Imaging Proportional Counter (IPC) or High Resolution Imager (HRI) on the *Einstein Observatory*. The IPC has a lower background rate than the HRI and so is the more sensitive detector but it has a poorer spatial resolution. We study here those clusters with particularly good data for which other work (Arnaud 1985; Arnaud & Fabian 1987) suggests the presence of a cooling flow. The clusters and their properties are listed in Table 1. We have included neither the Perseus cluster (A426) nor the Virgo cluster as the removal of their central point source creates additional uncertainties.

Table 1. The input parameters for the clusters. The columns are as follows: (i) name of the cluster; (ii) redshift from the compilation by Sarazin (1986), or # Schmidt (1986); (iii) distance in Mpc assuming a Hubble flow and $H_0=50$ km s^{-1} Mpc^{-1}; (iv) line-of-sight cluster velocity dispersion in kms^{-1} – most are from the compilation by Quintana & Melnick (1982), except # Quintana *et al.* (1985), [ ] reduced from the value of 1440 in Jones & Forman (1984) in order that the deprojection could reach a sufficiently low temperature, ⟨ ⟩ arbitrarily assigned as there are no velocity dispersions in the literature; (v) core radii in Mpc from Sarazin (1986) or ⟨ ⟩ arbitrarily assigned at 0.4; (vi) galactic column density in units of 10^{21} cm^{-2} from the survey by Stark *et al.* (in preparation); (vii) mean temperature for the X-ray emission in keV – most are from the cluster deprojection survey by Arnaud (1987), except # Jones & Forman (1984), $ Rothenflug & Arnaud (1985), % Singh, Westergaard & Schnoppper (1986) and * Arnaud *et al.* (1987).

Name	z	Dist.	σ	Core	N_H	Temp.
A 85	.0518	310.8	[1300]	<0.4>	0.39	6.8
A 262	.0164	98.4	415	<0.4>	0.63	2.4 #
A 478	.09	540.	<750>	0.20	1.21	7.3 $
A 496	.0316	189.6	657 #	<0.4>	0.43	5.75
A 1060	.0114	68.4	777	0.24	0.58	3.2 %
Cen.	.0107 #	64.2	870	<0.4>	0.88	2.3
MKW 3s	.045 #	270.	<600>	<0.4>	0.38	3.2
A 2063	.0337	202.2	521	<0.4>	0.36	4.4
A 2199	.0305	183.0	784	0.22	0.10	3.6
A 2244	.0997	598.2	<750>	0.4	0.27	6.5
Cyg A	.0575 #	345.	<750>	<0.4>	1.00	4.1 *

The X-ray counts in each image are separated into annuli centred on the peak of emission and then deprojected, following the method outlined by Fabian *et al.* (1981), to yield count emissivities in spherical shells at the cluster. Here we introduce a new method of analysis (the multiphase method, MM, discussed in Section 3) which apportions these count emissivities to several gas density phases within each shell. Previously we have assumed that the gas is represented by a single density and temperature at each radius (here called the single-phase method, SM). Then, given that the emission is due to thermal bremsstrahlung, recombination radiation and line emission (we use the code of Raymond & Smith 1977) and that the gas pressure distribution is hydrostatic, we can solve for the density and temperature within each shell. We include photoelectric absorption using values from the compilation of galactic H I by Stark *et al.*

(in preparation) and the cross-sections of Morrison & McCammon (1983). The pressure is fixed by requiring that the emission-weighted temperature of the gas agrees with measured values, or with correlations of these values. In the few cases where both HRI and IPC data are available we match the HRI pressure to that of the IPC.

In order to estimate the mass deposition rate in the SM we split the count rate into two. One part is from the gas flowing across the shell liberating thermal and potential energy, and the other is from gas which is deposited uniformly in volume within the shell (see Thomas 1986). Starting at the centre and working outwards we calculate the mass deposition needed within each shell to supply the observed luminosity. This is a simple analogue of our new method, the MM.

The analysis requires knowledge of the gravitational potential distribution within the centre of the cluster. For this we adopt a King (1966) model for the distribution of cluster matter. The velocity dispersons and core radii are given in Table 1. The galaxy potential is unimportant except in the HRI and initially we adopted standard values of a velocity dispersion of 250 km s^{-1} and a core radius of 300 pc. As described in the text we later replaced the galaxy potential with a massive halo of 10^{11} $M_\odot$ kpc^{-1}.

3 The multiphase method for determining flow properties

We treat the inhomogeneous gas as being made up of a finite number of homogeneous phases. The flow is assumed to be comoving and steady. We discuss in Section 7 the possibility that the gas does not comove. The flow becomes unsteady outside the radius where the cooling time of the hottest phase exceeds the age of the flow (assumed to be H_0^{-1}). We assume that it only introduces substantial errors, however, outside the radius where more than about half the count rate comes from gas with a cooling time exceeding H_0^{-1} (we take H_0=50 km s^{-1} Mpc^{-1}). This is discussed further in Sections 5 and 6. Mass injection is taken as negligible throughout the flow, so that the assumption of a steady state makes the mass flow rate in each of the phases independent of the radius. The radial variation of the total mass flow rate is modelled by the removal of each phase from the flow as its cools to T=0.

The deprojection of the data to yield the count emissivity profile divides the region into spherical shells. Within each of these shells the pressure is taken as constant. Thus the inflow is modelled as successive cycles of constant pressure cooling followed by adiabatic compression as the gas moves from one shell to the next. The constant pressure cooling rate is given by

$$\frac{dT}{dt}=-\frac{2}{5}\frac{p\Lambda_c(T)}{kT}, \tag{1}$$

where T is the temperature, p is the pressure divided by Boltzmann's constant, and for convenience we have rescaled the cooling function, Λ, to (e.g. Raymond, Cox & Smith 1976)

$$\Lambda_c=\frac{n_e n_H}{n_T^2}\Lambda\approx 0.229\Lambda, \tag{2}$$

where n_e, n_H and n_T are, respectively, the electron, photon and total particle number densities.

If the gas in the ith phase cools from temperature $T_{i,j}$ to $T'_{i,j-1}$ in passing through the jth shell, then the time it spends in that shell is (from equation 1)

$$\delta t_j=\frac{5}{2}\frac{k}{p_j}[F(T_{i,j})-F(T'_{i,j-1})], \tag{3}$$

where p_j is the value of p in the jth shell and

$$F(T)=\int_0^T \frac{T'\,dT'}{\Lambda_c(T')}. \tag{4}$$

Since the flow is comoving δt_j is the same for all gas phases in the shell. Any phase which drops out, that is cools to $T=0$, in the jth shell then does so at the inner boundary of that shell.

The emission detector function, $\xi(T)$, is defined by requiring that $\xi(T)p^2$ is the count emissivity, i.e. the total count in the detector from a unit volume of gas in the source at temperature T and pressure p. ξ contains all the effects of the emission spectrum, source distance, photoelectric absorption, exposure and detector response, folded together. If the mass flow rate in the ith phase is $\dot{M}_i$, then the number of counts contributed by this phase from the jth shell is

$$C_{i,j}=\frac{5}{2}\frac{\dot{M}_i k}{\mu m_{\rm H}}[H(T_{i,j})-H(T'_{i,j-1})], \tag{5}$$

where $\mu m_{\rm H}$ is the mean mass per particle and

$$H(T)=\int_0^T \frac{T'^2\xi(T')\,dT'}{\Lambda_{\rm c}(T')}. \tag{6}$$

The volume occupied by ith phase as it flows through the jth shell is

$$V_{i,j}=\frac{5}{2}\frac{\dot{M}_i k}{p_j^2\mu m_{\rm H}}[J(T_{i,j})-J(T'_{i,j})], \tag{7}$$

where

$$J(T)=\int_0^T \frac{T'^2\,dT'}{\Lambda_{\rm c}(T')}. \tag{8}$$

The total count, C_j from the jth shell is determined, as for the single-phase method, using the deprojection method of Fabian *et al.* (1981). The volume V_j of the shell is fixed by the geometry.

The multiphase flow solution is computed by working out from the centre and adding one new phase, representing the gas which cools to $T=0$, in each shell. Thus by the jth shell the mass flow rates $\dot{M}_1, \ldots, \dot{M}_{j-1}$ and the temperatures $T_{1,j-1}, \ldots, T_{j-1,j-1}$ are already determined. Given an estimate for p_j, the temperature of each phase at the inner edge of the jth shell is determined by adiabatic decompression as

$$T'_{i,j-1}=\left(\frac{p_j}{p_{j-1}}\right)^{0.4} T_{i,j-1}. \tag{9}$$

Taking a value for δt_j and fixing $T'_{j,j}=0$ then determines $T_{1,j}, \ldots, T_{j,j}$ from equation (3). The total count emissivity must equal the sum of those from the individual phases so that

$$C_j=\sum_{i=1}^{j} C_{i,j}, \tag{10}$$

which gives a value for $\dot{M}_j$. Using all these quantities, the total volume of the gas in the shell is

$$V'_j=\sum_{i=1}^{j} V_{i,j}, \tag{11}$$

which does not generally equal V_j. The value of δt_j is then iterated until $V'_j=V_j$.

The mean density in jth shell is

$$\bar{\rho}_j=\left(\sum_{i=1}^{j}\dot{M}_i\right)\frac{\delta t_j}{V_j}. \tag{12}$$

We iterate on p_j until the equation of hydrostatic support is satisfied:

$$p_j = p_{j-1} - \tfrac{1}{4}(\bar{\varrho}_j + \bar{\varrho}_{j-1}) \frac{GM_{j-1}}{r_{j-1}^2} (r_j - r_{j-2}), \tag{13}$$

where r_j is the radius of the outer boundary of the jth shell and M_j is the gravitating mass inside r_j. The complete procedure for stepping the flow solution outward by one shell thus involves a double iteration. We vary the central pressure, which is the only free parameter with a fixed gravitational potential, to give pressure profiles matching those obtained by the deprojections. This then gives a mean temperature profile similar to that from the single-phase method which, in turn, has been related to the observed cluster temperature.

The integrals for F, J and H are tabulated using data from the code of Raymond & Smith (1977) and calibration data for the *Einstein Observatory*. Intermediate values are found by linear interpolation on the tables.

The values for $\dot{M}_i$ depend differentially on the counts, C_i, from the ith shell. For this reason the MM can only be applied to high quality data from the centre of bright clusters.

4 Comparison of multiphase method with single-phase results

In order to test the MM we analysed the clusters A 2199 and A 496 in detail. For both there are good IPC and HRI data and measured X-ray temperatures and optical velocity dispersions. The input parameters are listed in Table 1, and the available X-ray data in Table 2. Further details of the X-ray observations can be found in Arnaud (1987).

Table 2. Summary of the data on the clusters we analyse in this paper. The columns contain the cluster name, and the number of useful, annular, data bins, the binsize in arcsec and the binsize in kpc, for both the IPC and the HRI data. Further details of the X-ray observations can be found in Arnaud (1987).

	IPC			HRI		
Name	#	"	kpc	#	"	kpc
A 85	13	48	72			
A 262	10	48	23			
A 478	6	24	63	5	25	65
A 496	7	24	22	12	10	9
A 1060	13	48	16			
Cen.	11	48	15	11	20	6
MKW 3s	6	32	42	11	16	21
A 2063	7	48	47			
A 2199	8	48	43	6	20	18
A 2244	7	24	70	9	15	44
Cyg A	6	30	47	7	10	16

The IPC data were analysed with the SM using the observed mean temperature as a constraint. When analysing the HRI data the pressure profile was then matched to that of the IPC. The MM is only applicable to high quality data near the cluster centres, so it is not possible to constrain it using mean observed temperatures. Instead we normalized the pressure (and hence temperature) profile to match that from the SM.

We compare the results of the MM with those from the SM for A 2199 in Figs 1–4. The flow time of the least dense phase in the MM, which is the total flow time to the centre from that radius, is typically twice as large as the cooling time deduced in the SM. This is because it measures the cooling time of the hottest gas at the outside of the bin whereas the SM measures the mean cooling

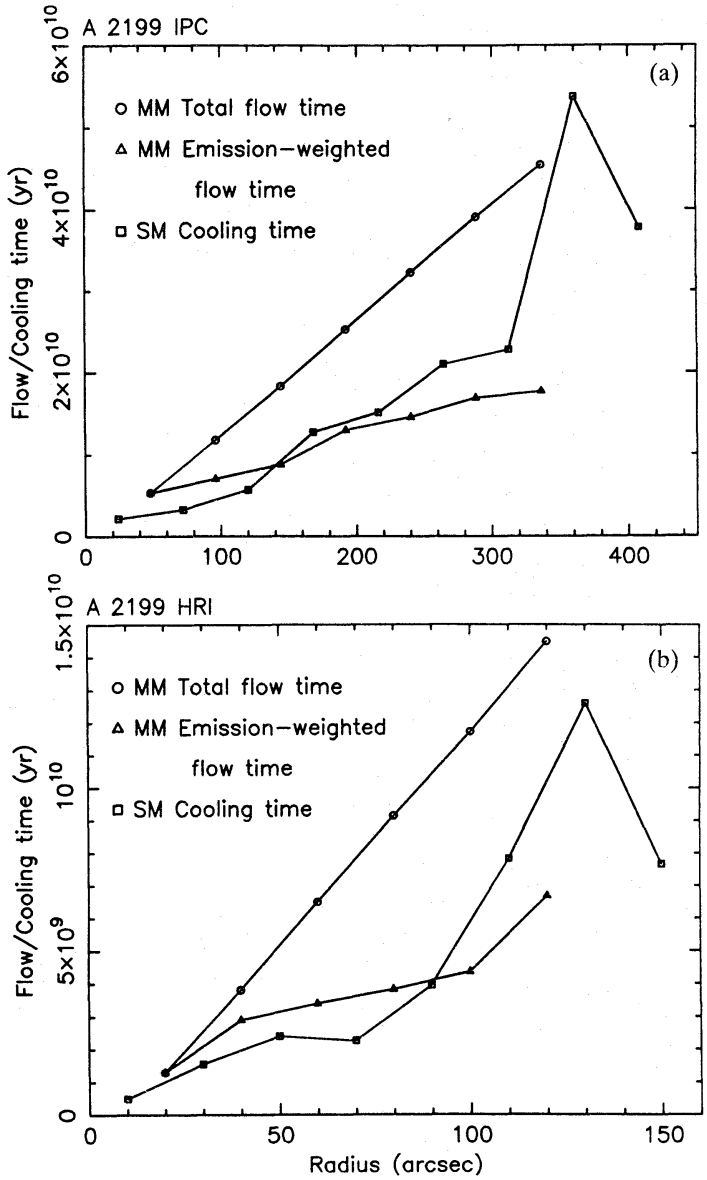

Figure 1. (a) A comparison of the cooling times deduced from the IPC data of A2199 using the single-phase method with the total, and emission-weighted, flow times from the multiphase method. (b) As (a) but for the HRI data.

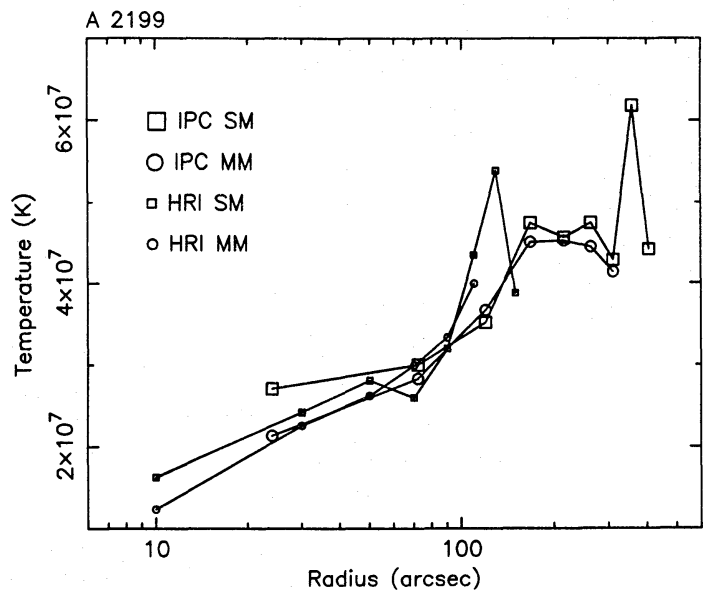

Figure 2. The temperature profiles for A2199 obtained with the single-phase and multiphase methods.

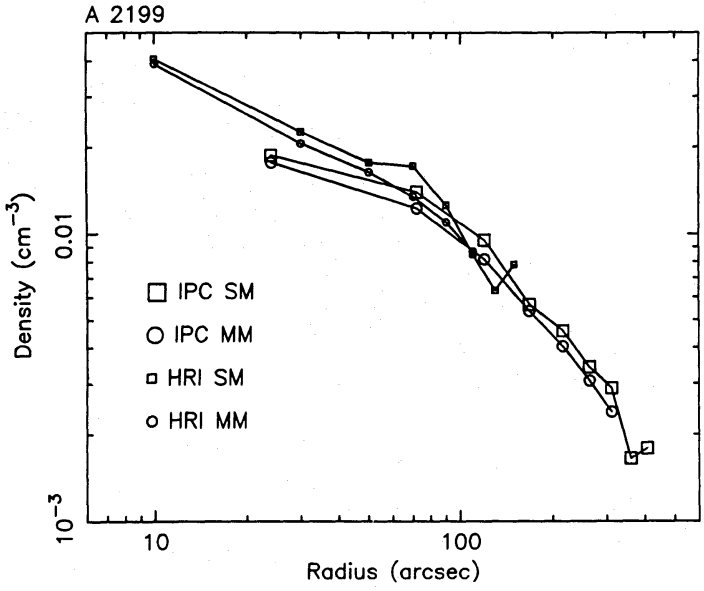

Figure 3. The density profiles for A2199 obtained with the single-phase and multiphase methods.

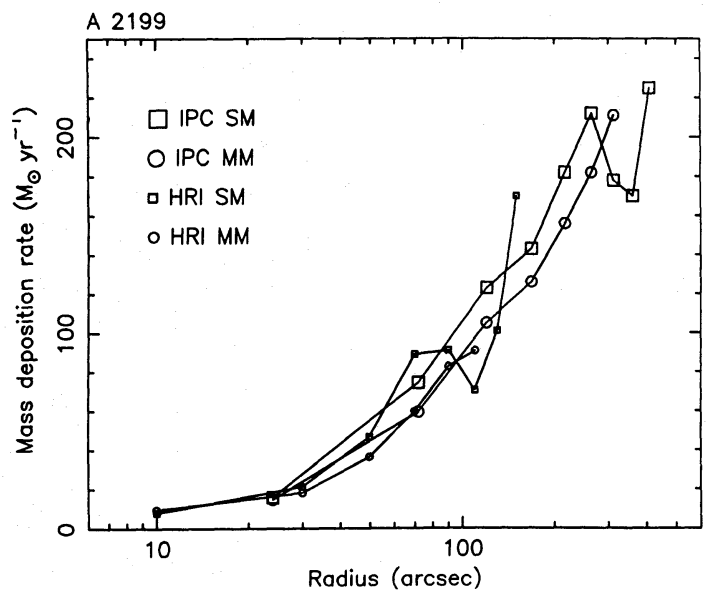

Figure 4. The mass deposition profiles, $\dot{M}(<r)$, (which equal the local mass inflow rate in a steady state) for A2199 as obtained with the single-phase and multiphase methods.

time of all the gas in the bin. We also plot the flow time for phases to cool to zero temperature, weighted by their contribution to the count rate at that radius. This emission-weighted flow time agrees well with the mean cooling time deduced from the SM.

The mean temperature plotted in Fig. 2 is given by $\Sigma\dot{M}_i T_i/(\Sigma\dot{M}_i)$ where T_i is the mean of the temperatures at the inside and outside of a bin. It agrees with $p/\bar{\varrho}$ (see equation 12).

The mass deposition profiles $\dot{M}(r)$ are in remarkably good agreement. A change in temperature should approximately result in a scaling of $\dot{M}(r)$ which keeps the energy flux, $\propto\dot{M}T$, fixed. We do not attempt to quote a total mass inflow rate for the cluster as this requires an outer limit to the flow. In the SM the 'cooling radius' is often taken to be the outer radius within which the cooling time is less than a Hubble time. However this is not a certain quantity but depends upon the binning and the adopted temperature. In the MM the 'cooling radius' is still less well defined because of the range of flow times for the different phases. The highest density gas may well cool and deposit mass over a volume very much larger than that contained within the 'cooling radius' found with the SM.

A 496 shows similar agreement between the MM and the SM. We conclude both that we have implemented the MM correctly and that the single phase treatment of the gas in the SM is a useful one.

5 The density distributions

We first note that the IPC point spread function has an angular size of about 70–100 arcsec half-width at half power (hwhp; Mauche & Gorenstein 1986). Some of the X-ray counts from the inner annuli will thus be shared with those further out. This limits the useful binsize of the IPC data. We choose the smallest size that gave a reasonably smooth count profile; a larger size would give too few bins for our purposes. The HRI data are much less affected by this problem as the hwhp is about 10 arcsec.

We work with the volume fraction distribution (vf) of the density, $f(\varrho, r)\, d\varrho$, which is the fraction of the volume at radius r that contains gas in the density range ϱ to $\varrho+d\varrho$. In Appendix A we derive the form of an evolving density distribution without solving the full equations given in Paper I. The important thing to note is that after some evolution has occurred there is a high-density tail which follows $f\sim\varrho^{-(4-\alpha)}$. This is also shown, more intuitively, in equations (22) and (23) of Paper I. It holds independently of the initial distribution and we should expect to see it in our results. The vf in the cluster is simply given by $f_i=\dot{M}_i T_{i,n}/(\Sigma \dot{M}_j T_{j,n})$ in the required bin. We fit the distribution of the cumulative volume fraction (cvf), $\Sigma_{j=1}^{i} f_j$, using a normalized density $\varrho_{i,n}/(\Sigma f_j \varrho_{j,n})$ as ordinate. The model distributions we use are

$$\text{cvf}=\begin{cases} 0, & \varrho<\varrho_m \\ A\left[1-\left(\dfrac{\varrho_m}{\varrho}\right)^{\beta}\right]^{k}, & \varrho\geq\varrho_m \end{cases} \tag{14}$$

and

$$\text{cvf}=A\ \exp\left[-\left(\frac{\varrho_0}{\varrho}\right)^{\beta}\right]. \tag{15}$$

These both give an asymptotic tail at high densities of $f\sim\varrho^{-(\beta+1)}$ and so we expect $\beta=3-\alpha$, ranging from 2.5 at temperature above 3×10^7 K up to 3.5 at lower temperatures. The normalization, A, should be close to, but not exactly, unity since the cvf reaches one at a finite value. We leave A free so as not to overconstrain β. ϱ_m is simply the lower density cut-off, whereas k determines the shape of the distribution at low densities. Where there is only a gradual rise in this region, ϱ_m and k are together unconstrained and we replace them with one parameter, ϱ_0, in model (15). Note that these distributions are fitted to the cumulative volume distribution and not the cumulative mass distribution as in Paper I.

We choose to examine the density distribution at the outer radius or the radius where the emission-weighted cooling time reaches 2×10^{10} yr (H_0^{-1}). This means that the high density phases always have cooling times of less than a Hubble time. In most cases, however, the cooling time of the least dense phases is larger than a Hubble time. This has two effects: it invalidates our assumption of a steady state, and the method will evolve the low-density phases back past the highest temperature of the initial gas distribution thus artificially increasing their volume fraction. The errors in the number of counts assigned to the high-density phases will be small but those in the low-density part of the inferred density distribution may not be. The four HRI data sets for which this effect is least important (A 496, Centaurus, MKW 3s and Cygnus A) do, however, appear similar to the others.

The best data set comprises the HRI data of A 496. Here the total flow time is less than a Hubble time throughout and so the steady-state assumption should hold. The results of our fits to the outer volume fraction distribution, which is shown in the upper panel of Fig. 5, are given in Table 3. The value of β is clearly too large and reflects the sharp transition from a narrow low-density spike to the high-density tail. This shape is difficult to explain. The cooling which must have taken place in order to produce the high-density tail would have been sufficient to spread out a narrow low-density peak. It would seem to imply that the matter forming the peak has been injected into the flow at this point. In other words it is not possible for a volume fraction distribution to have a tail steeper than that implied by equation (A7) of Appendix A unless the onset of cooling is comparatively recent (i.e. within the last few 10^9 yr). The volume fraction would then be determined by initial conditions.

One solution to this problem is the addition of a massive halo to the galaxy potential. This has the effect of increasing the gravitational work done on the gas flowing into the central regions so reducing the amount of cooling gas required to give the observed count emissivity. There is only a small effect at large radii where the potential is dominated by the cluster. A halo is expected since it is required in order to bind the hot gas both in isolated ellipticals (Forman, Jones & Tucker 1985; Thomas 1986; Fabian *et al.* 1986) and in central cluster galaxies such as M87 (Fabricant & Gorenstein 1983; Stewart *et al.* 1984; see also Mould, Oke & Nemec 1987; Huchra & Bodie 1987). The gravitational potential, and hence the mass, could be deduced if we knew the temperature profile of a cluster. Unfortunately spatially resolved X-ray spectra are not available for any of the clusters in our sample. The best we can do is use theoretical models of gas flows to constrain the acceptable range of temperature profiles. For a single-phase, constant pressure inflow the temperature is proportional to $r^{3/(3-\alpha)} \approx r^{1.2}$. This is the steepest possible temperature gradient. In a gravity-dominated flow the gas is heated or cools to of order the virial temperature as it moves inwards. The removal of cooled, low-entropy gas in the multiphase case will decrease the temperature gradient, but even so the temperature should not rise much above the virial temperature as the gas flows in.

To investigate whether a halo is present in A 496 we replace the galaxy potential with a halo of $10^{11} M_\odot$ kpc^{-1}, similar to that of M87. The new vf is shown in the lower part of Fig. 5(a). Note that the vertical scale has been doubled relative to the upper panel. Clearly the low-density spike has been smoothed out. Also the model fit (Table 3) now gives a value of β consistent with the cooling function. Without a halo the temperature decreases by a factor of 4 from 2.4×10^7 K at 100 kpc to 6×10^6 K at 10 kpc. This inner value is only just above the lower limit set by the galaxy potential although the temperature gradient is not steep enough to violate the constraint given above. With the inclusion of a halo the temperature profile becomes almost constant.

Similar conclusions hold for many of the other clusters. A list of clusters and the data used are given in Tables 1 and 2. In general these too show narrow low-density spikes in their density distributions which join abruptly onto the high-density cooling tail. This is associated with values of β in the model fits which are too high. We discuss individual clusters below. Unless stated otherwise the haloes we use have the form $M(<r)=10^{11}(r/\mathrm{kpc})M_\odot$. In general the temperature profiles do not constrain the solution. They decrease inwards when no halo is present and are much flatter with one.

A 262. The fits to the density distribution (Table 3) imply a massive halo, although we have had to look at the distribution far outside the cooling radius in the non-halo case in order to get enough data points for a fit to our model.

A 1060. The deprojected count emissivity shows a drop in the central bin. This is not significant within the errors but leads to a high cooling time ($>2\times10^{10}$ yr) in the centre with shorter time-scales further out. We will ignore this central deficit. The fits to the density distribution are improved by the addition of a halo.

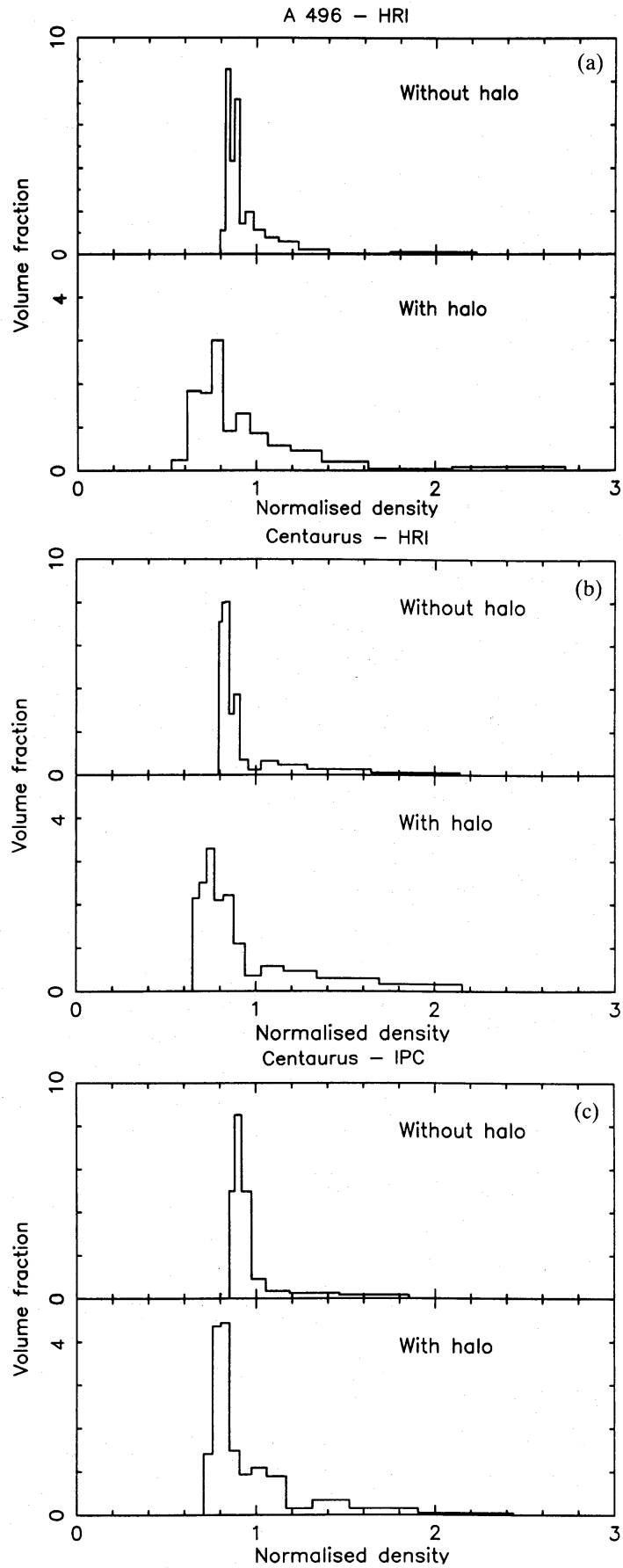

Figure 5. The volume fraction distributions at the outer edge of the useful data for (a) A 496 HRI, (b) Centaurus HRI and (c) Centaurus IPC. The upper and lower panels show the distribution with and without a massive halo in the gravitational potential respectively. Note that the vertical scales of the lower plots are twice those of the upper ones.

Table 3. Fits to the cumulative volume fraction distribution of the gas phases using either equation (15) or (16). The data sets not listed provided too few bins within the cooling region for a useful fit. The columns show respectively the cluster name, the instrument, the number of bins used in the fit and the best-fitting values of the various parameters. The second row for each entry gives the 90 per cent confidence range for the fits, obtained by assuming the fit has a reduced χ^2 of 1 and following the procedure outlined in Avni (1976). Notes: #, cooling time is $>2\times10^{10}$ yr; $, halo of $5\times10^{10}\,M_\odot$ kpc^{-1}.

Name			A	β	ρ_o	ρ_m	k
A 262	IPC	9#	1.01	4.8		0.88	0.4
			0.97 1.06	3.7 6.1			
A 262	IPC	10	1.08	3.2	0.81		
+halo			1.02 1.16	2.7 3.8			
A 496	HRI	12	0.99	5.0		0.83	0.5
			0.96 1.04	3.3 7.2		0.81 0.84	0.4 1.0
A 496	HRI	12	1.01	3.4		0.52	2.9
+halo			0.97 1.04	2.5 4.1		0.51 0.54	2.4 3.4
A 1060	IPC	7	1.03	4.1	0.77		
			1.00 1.06	3.7 4.4			
A 1060	IPC	9	1.07	2.5	0.72		
+halo			1.06 1.09	2.4 2.6			
Cen.	IPC	7	0.98	7.1		0.86	0.4
			0.91 1.13	3.6 12.2			
Cen.	IPC	11	1.03	3.0		0.73	0.7
+halo	$		0.98 1.10	2.0 4.0			
Cen.	HRI	11	1.03	2.7		0.79	0.4
			0.94 1.23	1.0 4.6			
Cen.	HRI	11	1.09	2.1		0.65	0.8
+halo	$		1.00 1.26	1.3 3.0			
MKW 3s	HRI	5	Too few bins to fit				
MKW 3s	HRI	11	0.99	4.1	0.77		
+halo			0.94 1.04	3.5 4.7			

Centaurus. This is another example where the total flow time throughout the HRI data and most of the IPC data is less than a Hubble time. The IPC data would seem to imply a halo, whereas the HRI data give values of β which become too low as the size of the halo is increased. The inner temperature in the non-halo case is again very low, 5×10^6 K. We compromise by using a halo of mass $5\times10^{10}\,M_\odot$ kpc^{-1}, half that above. The volume fraction distributions are shown in Fig. 5.

MKW 3s. With no halo we find that our method cannot extend beyond the inner five bins of the HRI data. This suggests, as for a large value of β in our fits, that too large a mass flow rate is attributed to the central bins. With a halo the solution can be extended out much further and β is acceptable.

Others. The other clusters have too few bins within the cooling radius to allow a reliable fit to the vf. In Fig. 6 we show on one plot the volume fractions obtained from all the data sets, (a) without a massive halo, and (b) with one. The latter lies closer to our theoretical expectation of a $f\sim\varrho^{-(4-\alpha)}$ high-density tail showing that, taken as a whole, the sample is better fit with the inclusion of a halo.

6 Mass deposition profiles

The mass deposition profiles, $\dot{M}(<r)$, of all the clusters are shown in Fig. 7. The gravitational potential includes a massive halo of $10^{11}\,M_\odot$ kpc^{-1} except in the case of Centaurus where half this

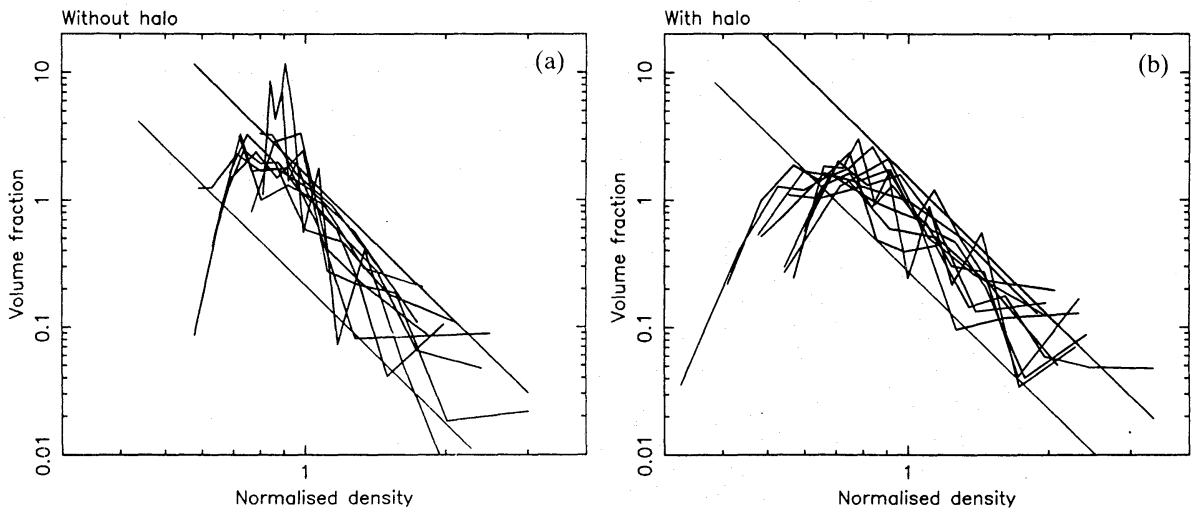

Figure 6. The volume fraction distributions for those data sets listed in Table 2 (a) without, and (b) with, a halo contribution to the gravitational potential. The straight lines have a slope of −3.6 corresponding to the expected distribution at high densities. Inclusion of a dark halo clearly brings the results closer to the theoretical predictions. Note that most of the volume fraction distributions rise at the highest-density point. This is simply because fluctuations which cause the volume fraction to dip below zero in any bin force us to limit our results to the previous one.

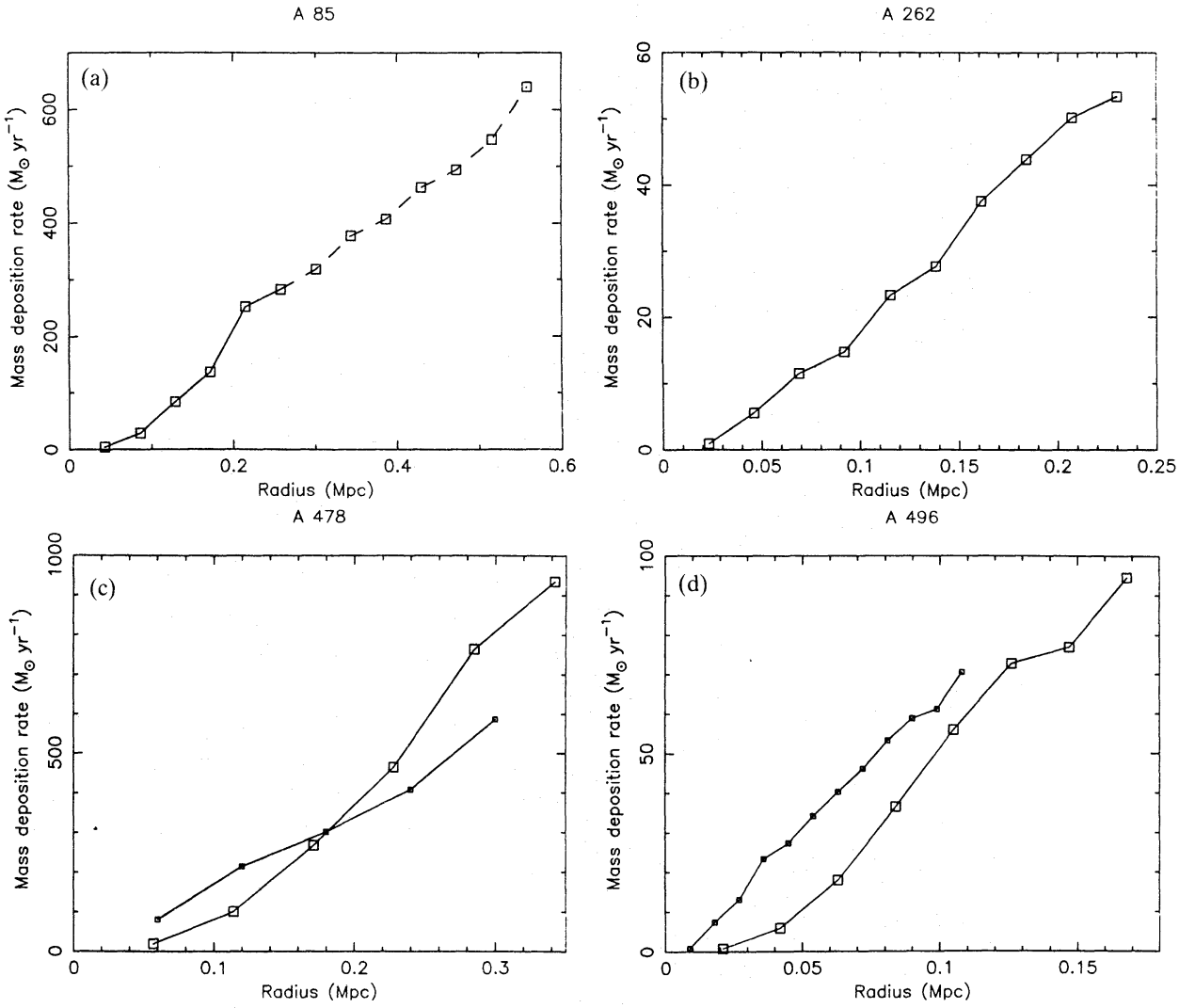

Figure 7. Mass deposition profiles for all the clusters studied here. The potential includes a massive halo. The flattening towards the centre, especially of the IPC profiles, is due to the point spread function of the instruments.

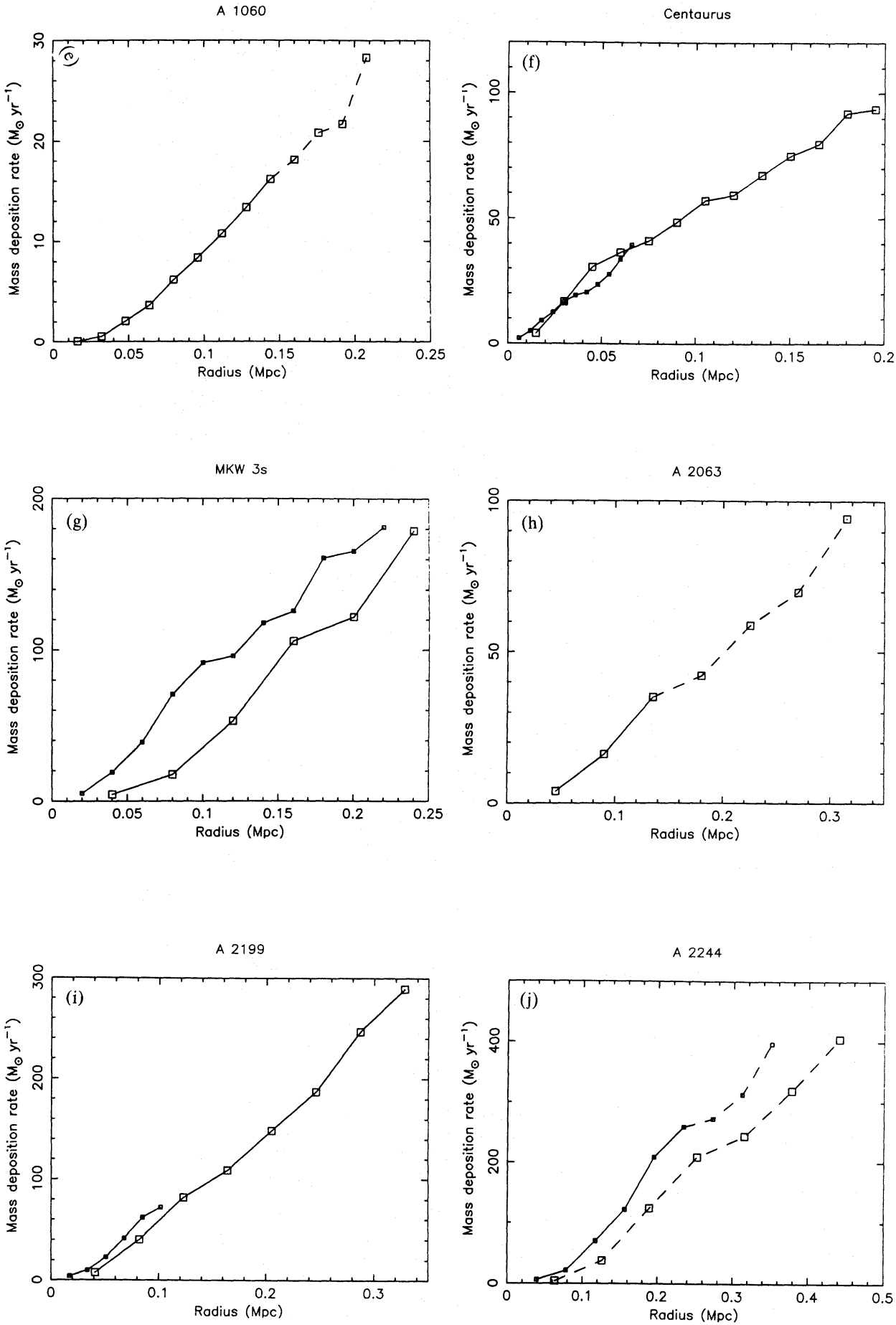

Figure 7–*continued*

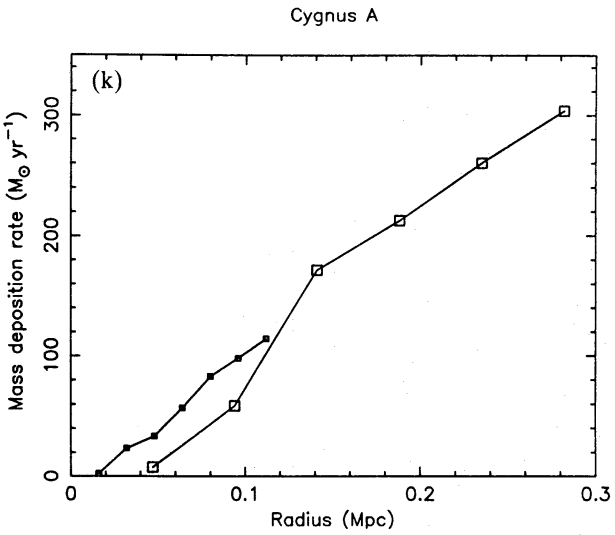

Figure 7–*continued*

value was used. The normalization of the profiles depends strongly on the temperature but the shape does not. In the absence of gravity the luminosity profile maps on to the mass-deposition with a $1/T$ scaling. Most of the profiles appear linear with some depression in the inner few bins. Formal fits to the profiles give $\dot{M} \propto r^m$ with m in the range 1–2 and approaching one as more data points are included. The lack of mass deposition in the centre is probably a consequence of the spatial resolution of the instruments, in particular the IPC. In those clusters for which we have data from both detectors the mass deposition rate from the IPC is depressed below that of the HRI in the centre of the cluster and rises towards it at a few arcmin. The data become too noisy and the MM begins to break down in the outer one or two bins of each plot. Mass deposition will not cut off sharply at the 'cooling radius' as some gas in the high-density tail is still cooling to low temperatures beyond it. For this reason we continue to plot the mass deposition rate outside this radius (with a dashed line) in Fig. 7. Unless there is a sharp discontinuity in the density distribution this will be a good approximation to the true profiles because the gas which has a long cooling time contributes only a minority of the counts. The mass deposition is extensive enough and at high enough rates to form the luminous envelopes of cD galaxies found at the centre of the flows, a possibility being investigated further by PAT.

7 Discussion

We have produced a self-consistent, multiphase method in which the peaked X-ray emission from a cluster core is produced by comoving gas phases at a range of densities (one for each data point) which cool in pressure equilibrium with each other. It gives good agreement with the single-phase deprojection method of Fabian *et al.* (1981). The SM can, therefore, be usefully applied to data which are too noisy for the MM. We find that, for the best data-sets, the tail of the density distribution from the MM does not agree with theoretical predictions unless we add a massive halo of order $10^{11}\,M_\odot\,\mathrm{kpc}^{-1}$ to the potential. This is of the same size as that needed to bind the hot gas. As the addition of a massive halo increases the temperature of the central gas, we have checked for convective stability of the resulting mean temperature. It is not violated in any case. The deduced mass deposition profiles rise approximately linearly with radius at rates of up to $100\,M_\odot\ \mathrm{yr}^{-1}$ within 100 kpc. This is not large enough to have formed the underlying dark halo within a Hubble time but could have a significant effect on the evolution of the central galaxy.

Unfortunately the data are not yet detailed enough to investigate our other goal, the initial distribution from which those we observe have evolved. We can say, nevertheless, that the spread

in densities that we infer is not excessive and could easily have arisen by cooling from an initial distribution ranging over, say, a factor of 2 in density.

The accumulation of cooled matter in a profile $\dot{M}(<r) \propto r$ which is similar to the dark halo distribution, and the detection of light from only a small fraction of whatever stars are formed from this matter (Fabian *et al.* 1982; Sarazin & O'Connell 1983; Johnstone, Fabian & Nulsen 1987) suggest that larger cooling flows in the past could have been directly responsible for the formation of the dark haloes (see also Fabian, Arnaud & Thomas 1986). This hypothesis requires that $\dot{M}(<r) \propto r$ is a general result for the distributions found in clusters. We show in Appendix B that the density distribution which consists entirely of the cooling tail discussed in Section 5 gives a mass-deposition profile of the correct form. We suggest that all initially narrow distributions will behave in the same way and postulate the following mechanism. Consider a uniform gas cloud that collapses under gravity to form a large galaxy and in doing so is heated to its virial temperature (see Rees & Ostriker 1977). Radiative cooling of the cloud leads to massive star formation in the core of the protogalaxy. This produces metals and, possibly with the onset of an active nucleus, much kinetic energy which then mixes and heats the flow leading to the creation of an inhomogeneous, metal-rich interstellar medium. The gas may be heated to such an extent that most of it is expelled from the galaxy, or it may be stripped during galaxy collisions, leading to the formation of the intracluster medium. The presence of iron in many clusters at half of solar abundance (Mushotzky 1984; Rothenflug & Arnaud 1985) is key evidence that such mixing is plausible. Buoyancy forces acting on the wide range of densities in the mixed gas will tend to reduce the local density contrast on a dynamical time-scale ($\sim 10^9$ yr). This may explain why we do not see very broad density distributions. Relative motions will, however, tend to disrupt gas blobs and reduce their length-scales so that their terminal velocities are small (see Paper I). Magnetic fields can also help to pin blobs to the mean flow. We have assumed here that after the initial turbulent mixing the phase comove and that dense blobs remain tied to the mean flow as they cool. The density variation remaining in the intracluster medium is sufficient to deposit gas over a wide range of radii.

Small amounts of dense gas will be found throughout the cluster, well beyond the radius where the mean cooling time equals a Hubble time. The multiphase method cannot be extended simply to these outer regions without introducing large errors from the unknown initial conditions in the slowly cooling, low-density gas. We could assume that the initial density distribution is similar at all radii and that the gas has cooled there *in situ* at constant pressure. Given the pressure profile and age of the system the problem is then to find the density distribution which would evolve under equation (A6) to give the observed luminosity profile. The quality of the data precludes such a scheme at present. A more detailed investigation of these questions must await spatially resolved X-ray spectra from *ROSAT*.

Acknowledgments

We thank Keith Arnaud for his help in developing the multiphase method. PAT acknowledges an SERC studentship. ACF thanks the Royal Society for support.

References

Arnaud, K. A., 1985. *PhD thesis*, University of Cambridge.
Arnaud, K. A., 1987. Preprint.
Arnaud, K. A. & Fabian, A. C., 1987. Preprint.
Arnaud, K. A., Johnstone, R. M., Fabian, A. C., Crawford, C. S., Nulsen, P. E. J., Shafer, R. A. & Mushotzky, R. F., 1987. *Mon. Not. R. astr. Soc.*, **227**, 241.
Avni, Y., 1976. *Astrophys. J.*, **210**, 642.

Fabian, A. C., Arnaud, K. A. & Thomas, P. A., 1986. In: *Proc. IAU Symp. No. 117*, p. 201, eds Kormendy, J. & Knapp, G. R., Reidel, Dordrecht.
Fabian, A. C., Nulsen, P. E. J. & Canizares, C. R., 1982. *Mon. Not. R. astr. Soc.*, **210,** 933.
Fabian, A. C., Nulsen, P. E. J. & Canizares, C. R., 1984. *Nature*, **310,** 733.
Fabian, A. C., Hu, E. M., Cowie, L. L. & Grindlay, J., 1981. *Astrophys. J.*, **248,** 47.
Fabian, A. C., Thomas, P. A., Fall, S. M. & White, R. E., 1986. *Mon. Not. R. astr. Soc.*, **221,** 1049.
Fabricant, D. & Gorenstein, P., 1983. *Mon. Not. R. astr. Soc.*, **267,** 535.
Forman, W., Jones, C. & Tucker, W., 1985. *Astrophys. J.*, **293,** 102.
Huchra, J. & Brodie, J., 1987. *Astrophys. J.*, in press.
Johnstone, R. M., Fabian, A. C. & Nulsen, P. E. J., 1987. *Mon. Not. R. astr. Soc.*, **224,** 75.
Jones, C. & Forman, W., 1984. *Astrophys. J.*, **276,** 38.
King, I. R., 1966. *Astr. J.*, **71,** 64.
Mauche, C. W. & Gorenstein, P., 1986. *Astrophys. J.*, **302,** 371.
Morrison, R. & McCammon, D., 1983. *Astrophys. J.*, **270,** 119.
Mould, J. R., Oke, J. B. & Nemec, J. M., 1987. *Astr. J.*, **92,** 53.
Mushotzky, R. F., 1984. *Phys. Scripta.*, **T7,** 151.
Nulsen, P. E. J., 1986. *Mon. Not. R. astr. Soc.*, **221,** 377.
Quintana, H. & Melnick, J., 1982. *Astr. J.*, **87,** 972.
Quintana, H., Melnick, J., Infante, L. & Thomas, B., 1985. *Astr. J.*, **90,** 410.
Raymond, J. C. & Smith, B. W., 1977. *Astrophys. J. Suppl.*, **37,** 419.
Raymond, J. C., Cox, D. C. & Smith, B. W., 1976. *Astrophys. J.*, **204,** 290.
Rees, M. J. & Ostriker, J. P., 1977. *Astrophys. J.*, **179,** 541.
Rothenflug, R. & Arnaud, M., 1985. *Astr. Astrophys.*, **144,** 431.
Sarazin, C. L., 1986. *Rev. mod. Phys.*, **58,** 1.
Sarazin, C. L. & O'Connell, R. W., 1983. *Astrophys. J.*, **268,** 552.
Schmidt, K.-H., 1986. *Astr. Nachr.*, **307,** 69.
Singh, K. P., Westergaard, N. J. & Schnopper, H. W., 1986. Preprint.
Stewart, G. C., Canizares, C. R., Fabian, A. C. & Nulsen, P. E. J., 1984. *Astrophys. J.*, **278,** 536.
Thomas, P. A., 1986. *Mon. Not. R. astr. Soc.*, **220,** 949.
White, R. E. & Sarazin, C. L., 1987a. *Astrophys. J.*, in press.
White, R. E. & Sarazin, C. L., 1987b. *Astrophys. J.*, in press.

Appendix A

Using the notation of Paper I we define $\Psi(\varrho, r)$ to be the mass inflow rate of gas with density less than ϱ at radius r. We refer everything to a reference radius R, (see Fig. A1). Mass conservation gives

$$\Psi(\varrho, r)=\Psi(\varrho_R; R), \tag{A1}$$

where $\varrho_R(\varrho, r)$ is the density at R of gas which has density ϱ at r. The gas flow can be expressed in terms of the critical density $\varrho_c(r; R)$ which is defined to be the density at R of gas which reaches infinite density at r. The volume fraction $f(\varrho, r)$ is given by

$$f(\varrho, r)=\frac{1}{4\pi r^2 \varrho u}\left.\frac{\partial \Psi}{\partial \varrho}\right|_r, \tag{A2}$$

where u is the velocity of inflow at radius r.
We have from equation (A1)

$$\left.\frac{\partial \Psi(\varrho, r)}{\partial \varrho}\right|_r=\left.\frac{\partial \Psi(\varrho_R; R)}{\partial \varrho_R}\right|_R \left.\frac{\partial \varrho_R}{\partial \varrho}\right|_r. \tag{A3}$$

Thus using equations (A2) and (A3) we get

$$f(\varrho, r)=\frac{R^2 u(R)}{r^2 u(r)} f(\varrho_R; R)\left.\frac{\partial \varrho_R}{\partial \varrho}\right|_r. \tag{A4}$$

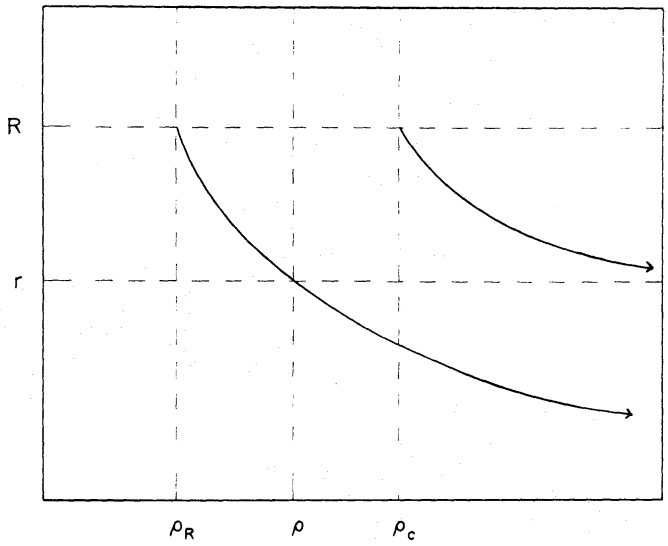

Figure A1. Streamlines in the ϱ, r plane. The variables at radius r are referred to those at reference radius R. The solution can be expressed in terms of $\varrho_c(r; R)$, the density at R whose streamline reaches infinite density at r.

The densities can be related by the cooling function, assumed proportional to T^{α} (see paper I):

$$\left(\frac{p^{0.6}}{\varrho}\right)^{2-\alpha} = \left(\frac{p_R^{0.6}}{\varrho_R}\right)^{2-\alpha} - \left(\frac{p_R^{0.6}}{\varrho_c}\right)^{2-\alpha}. \tag{A5}$$

Substituting equation (A5) in (A4) we obtain

$$f(\varrho, r)=\text{fn}\,(r)\times f\left\{\varrho\left(\frac{p_R}{p}\right)^{0.6}\left[1+\left(\frac{\varrho}{\tilde{\varrho}}\right)^{2-\alpha}\right]^{-1/(2-\alpha)};\ R\right\}\left[1+\left(\frac{\varrho}{\tilde{\varrho}}\right)^{2-\alpha}\right]^{-(4-\alpha)/(2-\alpha)}, \tag{A6}$$

where fn (r) is some function of r and $\tilde{\varrho}=\varrho_c(p/p_R)^{0.6}$. For $\varrho \gg \tilde{\varrho}$ we have

$$f(\varrho, r) \propto \frac{f(\varrho_c;\ R)}{\varrho^{4-\alpha}}. \tag{A7}$$

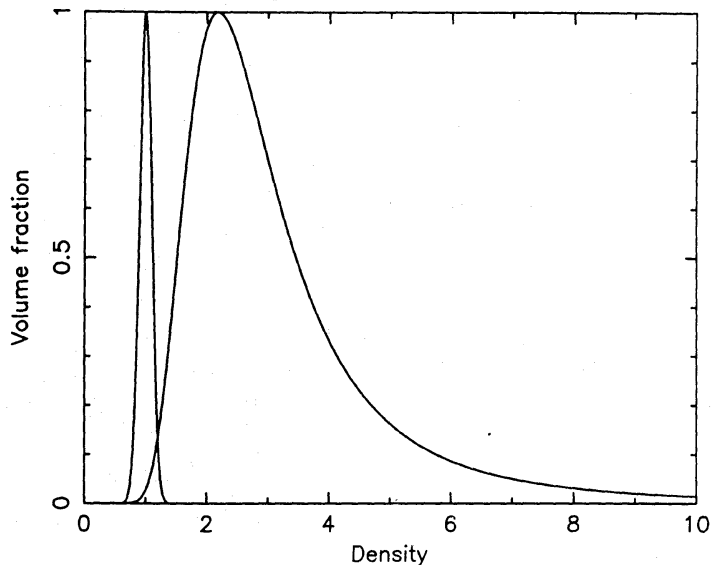

Figure A2. The left-hand curve shows a Gaussian volume fraction distribution with a width of one tenth of the mean density. The right-hand curve shows the corresponding distribution after cooling at constant pressure until approximately one fifth of the mass has been deposited. Both curves are normalized to a maximum of 1.

Thus after some cooling has taken place the volume fraction distribution develops a high-density tail whose shape is determined only by the cooling. As an example we show in Fig. A2 the distribution obtained by evolving a Gaussian profile at constant pressure to the point where approximately one fifth of the mass has cooled. An initially narrow density distribution which falls off faster than $f \propto \varrho^{-(4-\alpha)}$ at high densities will, by the time much of the gas has cooled, have developed a dominant $\varrho^{-(4-\alpha)}$ tail. More extended distributions, however, which fall off less quickly at high densities, will not form such a tail until much of their mass has been deposited.

Appendix B

We have shown in Appendix A that the evolution of a volume fraction, f, is simply expressed in terms of the critical density, ϱ_c, but the form of ϱ_c which determines the mass deposition profile $\dot{M}(r)$ is not in general easy to find. Nulsen (1986) has considered many analytic forms for f in detail. Here we present a highly simplified discussion for a stationary constant-pressure flow in which

$$f(\varrho, r)=\frac{(3-\alpha)\varrho_m^{3-\alpha}}{\varrho^{4-\alpha}}, \qquad \varrho>\varrho_m \tag{B1}$$

where the lower density cut-off, $\varrho_m(r)$, becomes infinite at $r=0$. It can be verified by substituting equation (B1) into equation (A6) that the form of f remains constant in time and only ϱ_m varies. The energy equation of the gas is

$$\frac{5}{2}\varrho k\frac{dT}{dt}=-\varrho^2\Lambda_0 T^{\alpha}. \tag{B2}$$

At constant pressure this gives

$$\dot{\varrho} \propto -u\frac{d\varrho}{dr} \propto \varrho^{3-\alpha}. \tag{B3}$$

The equation of conservation of mass for the gas is

$$\frac{\partial(\varrho f)}{\partial t}+\nabla\cdot(\varrho f\mathbf{u})+\frac{\partial(\varrho f\dot{\varrho})}{\partial\varrho}=0. \tag{B4}$$

The third term comes from the fact that we are treating the density phases separately. It has the same form in density space as the usual, second term above for the divergence in physical space. The first term is zero for a stationary flow and we have chosen the form of the distribution so that the third term in equation (B4) vanishes. Then setting the second term to zero gives, in spherical geometry

$$\varrho_m^{3-\alpha}r^2u=\text{const.} \tag{B5}$$

As the lower density cut-off, ϱ_m behaves in the same way as the other densities we can combine equations (B3) and (B5) to give

$$\varrho_m \propto r^{-3/(5-2\alpha)}, \tag{B6}$$

and hence

$$\dot{M} \propto r^2\varrho_m u \propto r^{3(2-\alpha)/(5-2\alpha)}. \tag{B7}$$

For α in the range -0.5 to 0.5, $\dot{M}\propto r^{\eta}$ where $\frac{9}{8}<\eta<\frac{5}{4}$. This means that density distributions that are dominated by a cooling tail, $f\propto\varrho^{-(4-\alpha)}$, will deposit matter in a manner that is almost linear in

radius. These correspond to the $\Psi=[1-(\varrho_m/\varrho)^{2-\alpha}]^k$ models of Paper I with small values of k. Distributions which do not rise as fast as $\varrho^{-(4-\alpha)}$ at low densities will have more extended mass deposition whilst those dominated by gravity will tend to be more peaked. Appendix A shows that almost any initially narrow density distribution will, by the time it has started to be deposited from the flow, have developed a dominant high-density tail. The width of the initial distribution determines how far it will flow in before this occurs, but inside this region the mass deposition profiles will be almost linear in radius. A high-density wing to the initial distribution will cause η to be more than one in the outer part of the flow whereas a low-density tail will cause η to be less than one in the centre. Further, preliminary analysis agrees with these statements.